





## Article

# Controlling the Structural Robustness of Zirconium-Based Metal Organic Frameworks for Efficient Adsorption on Tetracycline Antibiotics

Hee-Gon Kim <sup>1,2,†</sup>, Keunsu Choi <sup>3,†</sup> , Kibong Lee <sup>2</sup> , Soonjae Lee <sup>4</sup> , Kyung-Won Jung <sup>1,\*</sup> and Jae-Woo Choi <sup>1,5,\*</sup> 

<sup>1</sup> Water Cycle Research Center, Korea Institute of Science and Technology, Hwarang-ro 14-gil 5, Seongbuk-gu, Seoul 02792, Korea; 090923@kist.re.kr

<sup>2</sup> Department of Chemical and Biological Engineering, Korea University, Anam-ro 145, Seongbuk-gu, Seoul 02841, Korea; kibonglee@korea.ac.kr

<sup>3</sup> Department of Physics, Ulsan National Institute of Science and Technology, UNIST-gil 50, Ulju-gun, Ulsan 44919, Korea; c.keunsu@gmail.com

<sup>4</sup> Department of Earth and Environmental Sciences, Korea University, Anam-ro 145, Seongbuk-gu, Seoul 02841, Korea; soonjam@korea.ac.kr

<sup>5</sup> Division of Energy & Environment Technology, KIST School, Korea University of Science and Technology, Hwarang-ro 14-gil 5, Seongbuk-gu, Seoul 02792, Korea

\* Correspondence: kyungwonj@kist.re.kr (K.-W.J.); plead36@kist.re.kr (J.-W.C.)

† These authors contributed equally.



**Citation:** Kim, H.-G.; Choi, K.; Lee, K.; Lee, S.; Jung, K.-W.; Choi, J.-W. Controlling the Structural Robustness of Zirconium-Based Metal Organic Frameworks for Efficient Adsorption on Tetracycline Antibiotics. *Water* **2021**, *13*, 1869. <https://doi.org/10.3390/w13131869>

Academic Editor: Maurizio Barbieri

Received: 22 May 2021

Accepted: 2 July 2021

Published: 5 July 2021

**Publisher's Note:** MDPI stays neutral with regard to jurisdictional claims in published maps and institutional affiliations.



**Copyright:** © 2021 by the authors. Licensee MDPI, Basel, Switzerland. This article is an open access article distributed under the terms and conditions of the Creative Commons Attribution (CC BY) license (<https://creativecommons.org/licenses/by/4.0/>).

**Abstract:** Tetracyclines (TCs) are the most widely used antibiotics for the prevention and treatment of livestock diseases, but they are toxic to humans and have frequently been detected in water bodies. In this study, the physical and chemical properties of the zirconium-based metal organic framework (MOF) UiO-66 and its NH<sub>2</sub>-functionalized congener UiO-66-NH<sub>2</sub> were investigated along with batch TC adsorption tests to determine the effect of functionalization on TC removal. TC removal was highest at pH 3 and decreased with increasing pH. Pseudo-1st and pseudo-2nd-order kinetic models were used to study the adsorption equilibrium times, and Langmuir isotherm model was found to be more suitable than Freundlich model. The maximum uptake for UiO-66 and UiO-66-NH<sub>2</sub> was measured to be 93.6 and 76.5 mg/g, respectively. Unexpectedly, the TC adsorption capacity of UiO-66-NH<sub>2</sub> was observed to be lower than that of UiO-66. Density functional theory calculations revealed that the pore structures are irrelevant to TC adsorption, and that the -NH<sub>2</sub> functional group could weaken the structural robustness of UiO-66-NH<sub>2</sub>, causing a reduction in TC adsorption capacity. Accordingly, robust MOFs with zirconium-based metal clusters can be effectively applied for the treatment of antibiotics such as TC in water.

**Keywords:** density functional theory calculations; structural robustness; tetracycline; zirconium-based metal organic frameworks; NH<sub>2</sub> functional group

## 1. Introduction

Water is vital to all living things. With rapid industrial development, increasing amounts of contaminants are being released into the aquatic environment at high concentrations. As a result, water contamination has become a worldwide issue in recent decades. During this period, various industrial pollutants, including antibiotics, have frequently been found in both aquatic and soil environments due to the excessive use of medicines required for preserving human and animal health. These contaminants significantly impair the water quality [1,2]. Antibiotics have been widely used for the prevention and treatment of diseases in humans and livestock, and for promoting livestock growth. The increased and long-term use of antibiotics has contributed to the acceleration of environmental pollution. Further, the elimination of these antibiotics from water by conventional treatment

processes is difficult [1,3–7]. The widespread emergence of antibiotics has led to serious health and environmental problems stemming from the resistance of pathogenic bacterial microorganisms to the antibiotics, the toxicity of these antibiotics to microorganisms in the aquatic environment, and the resulting endocrine disruption of organisms [8–10].

In particular, tetracyclines (TCs) are the most widely used antibiotics for livestock across the world, and TC-based antibiotics are the most common broad-spectrum antibiotics. Owing to their low cost and high antibacterial activity, TCs are extensively used in veterinary medicine for preventing and treating livestock diseases and as a feed additive for promoting animal growth in livestock farms. However, the continued use of large amounts of TCs has led to the emergence of TC-resistant bacteria. Furthermore, most TCs are poorly absorbed by the human body and livestock. Upon entering the environment, TCs pose a threat to human health and the ecological balance [2,11]. While unmetabolized TCs enter the natural environment after being excreted from the body through urine and feces, there are a variety of other pathways by which TCs reach the environment, including hospital waste, compost, and livestock waste. Thus, TCs are becoming a global social issue because they are a nonpoint source of soil and river pollution. TCs have been frequently detected at trace concentrations in the aquatic environment. Owing to their toxicity in water, when TCs enter the natural environment, they pose a potential threat to the safety of humans and aquatic ecosystems [1,12–15]. Therefore, it is necessary to remove TCs from the waste streams before they are discharged in water. The stable tetracene ring structure of TCs, comprising four benzene rings, makes their removal difficult by conventional water-treatment processes. Thus, it is important to develop an effective treatment process for the removal of TCs from water [16,17].

In recent years, water-treatment technologies such as enzymatic degradation, oxidation, photochemical degradation, and adsorption have been widely used. Adsorption is one of the most competitive water-treatment technologies because of its operational simplicity, low cost, and lack of secondary contaminants [18]. However, conventional adsorbents have a relatively low surface area and limited active sites, which causes problems such as poor adsorption selectivity and low adsorption capacity. To overcome these limitations, the development of more effective adsorbents is necessary [8,19].

Metal organic frameworks (MOFs) are one-, two-, or three-dimensional porous crystalline materials comprising metal ions or clusters coordinated to organic ligands [20]. Since Yaghi et al.'s pioneering study [20], there has been widespread research on MOFs. Compared with traditional adsorbents, MOFs have several advantages such as a high specific surface area, tailorable pore structure, open metal sites, well-modified surface properties, and superstability. However, because MOFs have low stability in the aqueous phase, research has predominantly focused on the gas phase, catalysis, drug delivery carriers for nanomaterials, luminescence, and adsorption of organic molecules. To date, there has been little research on the removal of antibiotics using MOFs [8]. Zirconium (Zr(IV))-based MOFs are widely known for their outstanding stability in water compared to other MOFs based on different metal ions or clusters. Zr-based MOFs have strong ionic bonds that combine Zr(IV) and carboxylate O atoms. Furthermore, Zr-based MOFs are stable in acidic and alkaline conditions, thermally stable at temperatures up to 500 °C, and can maintain their crystal structure under high pressure. Therefore, Zr-based MOFs have significant potential for use as adsorbent materials in water [21–29]. Table S1 lists several studies dealing with the adsorption-based removal of TCs using various MOFs. UiO-66 is the most representative Zr-based MOF and consists of octahedral  $\text{Zr}_6\text{O}_4(\text{OH})_4$  clusters with terephthalic acid [30,31]. Commonly, MOFs have 4–6 organic linkers connected to the metal clusters. When one of the linkers is damaged, the pores can fatally collapse, leading to the formation of boundary defects. However, in the case of UiO-66, 12 organic linkers are connected to the metal clusters, making this compound very stable chemically and allowing it to maintain its structure well, even when a linker becomes damaged [32]. Furthermore, UiO-66-NH<sub>2</sub>, containing the amine functional group, is chemically stable and

can maintain its structure even at pH 1 [33]. In this study, the Zr-based MOFs UiO-66 and UiO-66-NH<sub>2</sub> (Figure S1) were synthesized and used for the removal of TCs from water.

## 2. Experimental Details

### 2.1. Reagents

Tetracycline (C<sub>22</sub>H<sub>24</sub>N<sub>2</sub>O<sub>8</sub>, MW: 444.43, purity > 98%) was purchased from Sigma-Aldrich (St. Louis, MO, USA). The synthesis of MOFs used Zr(IV) chloride (ZrCl<sub>4</sub>, MW: 233.04, purity > 99.99% trace metals basis, anhydrous grade; Sigma-Aldrich, St. Louis, MO, USA), N,N-dimethylformamide (DMF, MW: 73.09, purity > 99.8%; Sigma-Aldrich, St. Louis, MO, USA), and hydrochloric acid (HCl 37%; WAKO, Osaka, Japan). Terephthalic acid (benzene-1, 4-dicarboxylic acid, H<sub>2</sub>BDC, MW: 166.13, purity > 98%) and 2-aminoterephthalic acid (H<sub>2</sub>BDC-NH<sub>2</sub>, MW: 181.15, purity > 99%) were purchased from Sigma-Aldrich (St. Louis, MO, USA) for use as linkers. The MOFs were washed using DMF and ethyl alcohol (EtOH, purity > 99.9%, high-performance liquid chromatography (HPLC) grade; J.T. Baker, Philipsburg, NJ, USA). In addition, deionized (DI) water (resistivity of 18.2 MΩ cm<sup>-1</sup> at 25 °C) was used throughout the experiments. To adjust the pH value, HCl (37% HCl; WAKO, Osaka, Japan) and sodium hydroxide (NaOH; Samchun, Korea) were used. Magnesium chloride hexahydrate (MgCl<sub>2</sub> 6H<sub>2</sub>O, Showa, Japan), potassium chloride (KCl, Showa, Japan), calcium chloride (CaCl<sub>2</sub>, Sigma-Aldrich, USA), sodium nitrate (NaNO<sub>3</sub>, Sigma-Aldrich, USA) were used as ion sources. All chemical reagents were used directly without further purification.

### 2.2. Synthesis of Metal Organic Frameworks

The MOFs were synthesized using the following procedure, which is a modification of the method reported by Katz et al. [34] and Wang et al. [15]. ZrCl<sub>4</sub>, DMF (5 mL), and 37% HCl were mixed in a glass bottle using sonication (37 kHz, 100 power) for 20 min until they were fully dissolved. Then, DMF (10 mL), BDC for UiO-66, and BDC-NH<sub>2</sub> for UiO-66-NH<sub>2</sub> were added to the solution and mixed using sonication (37 kHz, 100 power) for 20 min until they were fully dissolved. The mixtures were stirred for 18 h and aged for 6 h at 80 °C in an oil bath. The precipitates were filtered and then thoroughly washed with DMF (2 × 30 mL) and ethyl alcohol (2 × 30 mL) to remove the residual solvents. Next, the MOFs were dried at 120 °C for 24 h in a vacuum, leading to UiO-66 being obtained as a white powder and UiO-66-NH<sub>2</sub> being obtained as a yellow powder (Figure S2). The reagent amounts used for the synthesis are listed in Table S2. The synthesized MOFs were characterized by field emission scanning electron microscopy (FE-SEM), X-ray diffraction (XRD), X-ray photoelectron spectroscopy (XPS), Brunauer-Emmett-Teller (BET) theory, and Fourier-transform infrared spectroscopy (FT-IR).

### 2.3. Characterization of MOFs

The specific surface areas of UiO-66 and UiO-66-NH<sub>2</sub> were determined using the BET method (Belsorp-mini 2, MicrotracBEL Crop, Osaka, Japan). The XRD patterns were obtained using a Dmax2500/PC diffractometer (Rigaku Crop, Tokyo, Japan) with a 2θ scan range recorded from 5–90° at a scan speed of 2°/min. The surface morphologies of UiO-66 and UiO-66-NH<sub>2</sub> before and after the reaction were observed by FE-SEM (Inspect F, FEI, Hillsboro, OR, USA) with an acceleration voltage of 10 kV. The FT-IR spectra of UiO-66 and UiO-66-NH<sub>2</sub> before and after the reaction were acquired using an FTIR spectrometer (Perkin Elmer, Waltham, MA, USA) in the 400–4000 cm<sup>-1</sup> range. The specific elemental surface contents and their valence states were analyzed using XPS (Thermo ESCALAB 250XI, Waltham, MA, USA).

### 2.4. Adsorption Experiments

All adsorption experiments, including those for studying the equilibrium, kinetics, pH effects, TC initial concentrations effects, and MOF dosage effects, were conducted in an incubator at 200 rpm with the temperature maintained at 25 °C. All batch experiments

were conducted in the dark to prevent potential photodegradation of the TC. Before the adsorption experiments, both UiO-66 and UiO-66-NH<sub>2</sub> were activated by drying in a vacuum oven for 12 h at 120 °C. The equilibrium tests were conducted in 50 mL conical tubes containing 40 mL of 50 mg L<sup>-1</sup> TC solution with 10 mg of MOFs for 24 h to investigate the adsorption of the TCs onto UiO-66 and UiO-66-NH<sub>2</sub>. The samples were analyzed by filtering through a 0.2-μm polytetrafluoroethylene (PTFE) filter after 15 min of treatment at 4200 rpm in a centrifuge. To determine the effect of pH on the adsorption capacity, the tests were carried out in 50 mL conical tubes containing 40 mL of 50 mg L<sup>-1</sup> TC solution with 10 mg of MOFs for 24 h. Before investigating the effect of pH, the pH of the TC solutions was adjusted to range from 3–9 by adding 0.1 M (mol L<sup>-1</sup>) HCl or 0.1 M NaOH. The point of zero charge (PZC) experiments were conducted without TCs in 250 mL flasks containing 30 mL of DI water with 90 mg of MOFs. The effect of the initial TC concentrations was investigated on the optimum pH. The initial concentrations of the TCs were set in the 10–100 mg L<sup>-1</sup> range for 24 h. The kinetic tests were implemented in 250 mL flasks containing 200 mL of 50 mg L<sup>-1</sup> TC solution with 50 mg of MOFs at pH 3, 6, and 9. In order to confirm the effect of ionic strength in the low concentration, the experiment was conducted in the presence of Mg<sup>2+</sup>, K<sup>+</sup>, Ca<sup>2+</sup>, and NO<sub>3</sub><sup>-</sup> at the same concentration under the TC 0.5 mg L<sup>-1</sup> condition. The containers comprising the TC solution were placed in an incubator and stirred. The samples were periodically withdrawn to determine the residual concentrations of the TC. The sampling volume was 1 mL, and the total variation of the TC solution volume due to sampling was less than 6%. After sampling 1 mL at each reaction time, the sample was filtered using a 0.2-μm PTFE syringe filter to remove the adsorbents, and then analyzed using HPLC. The tests were conducted in consideration of the adsorption potential of the TCs in the PTFE syringe filter, which is negligible. All experiments were performed in duplicate.

## 2.5. Analytical Methods

HPLC (Flexar, Perkin Elmer, Waltham, MA, USA) with an ultraviolet (UV) detector and a ZORBAX SB-C18 (5 μm, 4.6 × 150 mm, Agilent, Santa Clara, CA, USA) column was used to analyze the TCs. The wavelength of the UV detector was set at 355 nm. The optimized mobile phase for the analysis of TCs comprised acetonitrile (ACN; Merck K GaA, Darmstadt, Germany) (30%), methanol (MeOH, purity > 99.9%, HPLC grade; J.T. Baker, Philipsburg, NJ, USA) (20%), and 0.01 M aqueous oxalic acid solution (OA; Samchun, Seoul, Korea) (50%). The flow rate was maintained at 0.6 mL/min, and the sample injection volume was 10 μL. All samples were centrifuged at 4200 rpm for 15 min and filtered using 0.2-μm PTFT filters before analysis. The pH was measured with a benchtop pH meter (Orion Star A211, Thermo Scientific, Waltham, MA, USA).

## 2.6. Calculation Method

We conducted density functional theory (DFT) calculations using the Vienna ab initio Simulation Package (VASP) code [35,36]. We used the Perdew-Burke-Ernzerhof exchange-correlational functional with the generalized gradient approximation (GGA) method [37]. The pseudopotentials were generated based on the projector-augmented wave (PAW) method [38]. We considered only the gamma point and set the energy cut-off for the planewave basis to 500 eV. All of the structures were optimized with a force criterion of 0.03 eV/Å. To avoid interactions between molecules in the periodic cells, the dimensions of the periodic cells were set to 30 × 30 × 30 Å<sup>3</sup>. The charge amounts of the atoms were obtained from Bader charge analysis [39]. The figures obtained from the DFT calculations were drawn with the VESTA code [40].



### 3. Results and Discussion

#### 3.1. Characterizations of MOFs

##### 3.1.1. Brunauer-Emmett-Teller Analysis

BET analysis was conducted to study the interaction of the contaminants with the adsorbent surfaces. A high specific surface area of the adsorbent is important because it allows for greater adsorption of the contaminants. The porosity, pore size distribution, and specific surface areas of UiO-66 and UiO-66-NH<sub>2</sub> were determined using the N<sub>2</sub> adsorption-desorption analysis method. For UiO-66, the specific surface area was 1581 m<sup>2</sup>/g, total pore volume was 0.66 cm<sup>3</sup>/g, and pore diameter was 1.61 nm. For UiO-66-NH<sub>2</sub>, the specific surface area was 1415 m<sup>2</sup>/g, total pore volume was 0.59 cm<sup>3</sup>/g, and pore diameter was 1.61 nm. The specific surface area and total pore volume of UiO-66 were larger than those of UiO-66-NH<sub>2</sub>, whereas the pore diameter was the same for both MOFs. The results are presented in Table 1.

**Table 1.** BET, total pore volume, and mean pore diameter parameters for MOFs.

Sample	UiO-66	UiO-66-NH <sub>2</sub>
BET	1581 m <sup>2</sup> g <sup>−1</sup>	1415 m <sup>2</sup> g <sup>−1</sup>
Total pore volume (p/p <sub>0</sub> = 0.990)	0.66 cm <sup>3</sup> g <sup>−1</sup>	0.59 cm <sup>3</sup> g <sup>−1</sup>
Mean pore diameter	1.7931 nm	1.8759 nm

##### 3.1.2. XPS Analysis

XPS analysis was conducted to study the surface elemental composition of UiO-66 and UiO-66-NH<sub>2</sub> before and after the adsorption of TCs. Figure 1 shows the wide-scan XPS spectra of UiO-66 and UiO-66-NH<sub>2</sub> before and after the adsorption of TCs. The characteristic peaks of C, O, and Zr are present in the spectra, which agree with those reported previously [23,41]. Figure 2a,b shows the C1s and O1s XPS spectra of UiO-66 and UiO-66-NH<sub>2</sub> before and after the TC adsorption. The binding energies of C1s increased by 0.13 eV for UiO-66-NH<sub>2</sub>, whereas those of O1s decreased by 0.25 eV for UiO-66 and 0.13 eV for UiO-66-NH<sub>2</sub>. As shown in Figure 2c, the Zr3d XPS spectra of UiO-66 and UiO-66-NH<sub>2</sub> were deconvoluted into two individual peaks. For both UiO-66 and UiO-66-NH<sub>2</sub>, the binding energies of the two peaks of Zr3d increased by 0.12 eV and 0.13 eV before and after the TC adsorption, respectively. These results indicate the involvement of C, O, and Zr in the adsorption process.

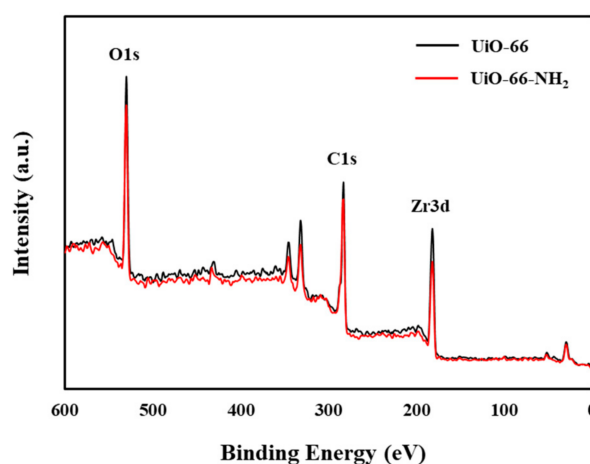


**Figure 1.** Complete XPS spectra of UiO-66 and UiO-66-NH<sub>2</sub>.

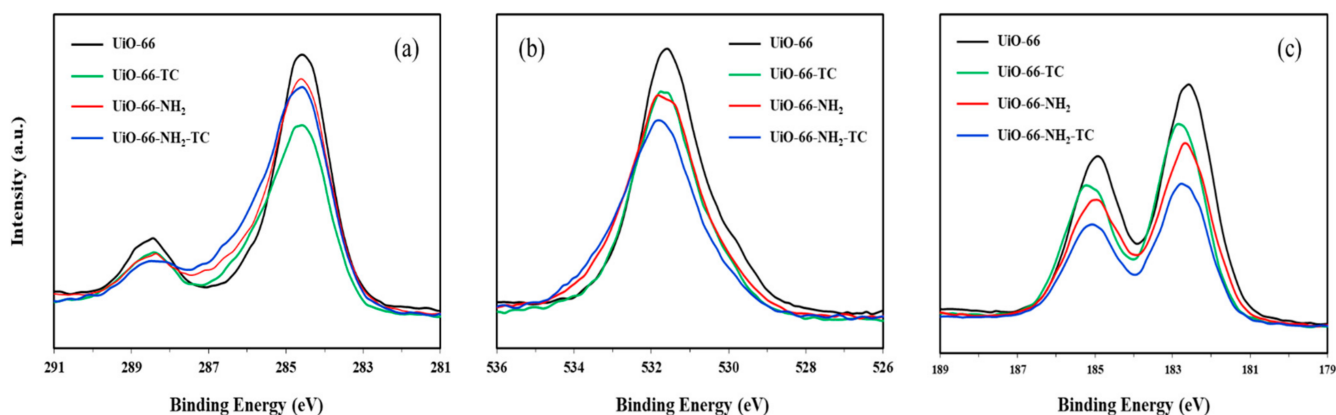


**Figure 2.** XPS spectra of UiO-66 and UiO-66-NH<sub>2</sub> before and after adsorption for (a) C1s, (b) O1s, (c) Zr3d.

### 3.1.3. Field Emission Scanning Electron Microscopy

The morphologies of UiO-66 and UiO-66-NH<sub>2</sub> before and after the reaction with the TCs are illustrated in Figure S3. The FE-SEM images of the unreacted UiO-66 and UiO-66-NH<sub>2</sub> presented an agglomerated, well-defined cube shape, in agreement with previous reports [23]. After adsorption of the TCs, the overall structures of UiO-66 and UiO-66-NH<sub>2</sub> remained similar, but became more aggregated with slightly smoother edges than before the reactions. In particular, after the reaction, UiO-66 showed a more aggregated shape than UiO-66-NH<sub>2</sub>. This suggests that UiO-66 has greater reactivity with the TCs than UiO-66-NH<sub>2</sub>. The diameters of both UiO-66 and UiO-66-NH<sub>2</sub> are generally in the 100–250 nm range before the reaction with the TCs, and in the 100–350 nm range after the reaction.

### 3.1.4. XRD Analysis

XRD analysis was carried out to confirm the synthesis of the MOFs and to investigate the crystalline structures of the MOFs before and after the TC adsorption. The XRD patterns of UiO-66 and UiO-66-NH<sub>2</sub> are presented in Figure 3. The characteristic peaks of the synthesized UiO-66 and UiO-66-NH<sub>2</sub> match the previously reported UiO-66 and UiO-66-NH<sub>2</sub> structures well, thus confirming the successful synthesis of UiO-66 and UiO-66-NH<sub>2</sub> [23,42,43]. The main peaks of UiO-66 before the TC adsorption were observed at  $2\theta$  values of 7.3°, 8.4°, 12.0°, 14.7°, 17.0°, 19.0°, 20.9°, 22.2°, 24.1°, 25.6°, 28.1°, 29.7°, 30.7°, 32.2°, 33.1°, and 34.4°, which correspond to the (111), (002), (022), (222), (004), (024), (115), (044), (135), (006), (335), (444), (117), (246), (355), and (008) crystal planes, respectively. The main peaks of UiO-66-NH<sub>2</sub> before the TC adsorption were observed at  $2\theta$  values of 7.3°, 8.4°, 12.0°, 14.7°, 17.0°, 19.0°, 20.9°, 22.2°, 25.7°, 28.1°, 29.7°, 30.7°, 32.2°, 33.0°, and 34.5°, which correspond to the (111), (002), (022), (222), (004), (024), (115), (044), (006), (335), (444), (117), (246), (355), and (008) crystal planes, respectively [44]. After functionalization with NH<sub>2</sub>, the characteristic peaks of UiO-66 were coterminous with those of UiO-66-NH<sub>2</sub>, indicating that the basic framework does not change during the incorporation of the functional groups into UiO-66. Furthermore, these results indicate that the UiO-66-NH<sub>2</sub> was well synthesized. After the TCs were adsorbed on UiO-66 and UiO-66-NH<sub>2</sub>, the XRD peaks of UiO-66-NH<sub>2</sub> disappear and broaden, indicating the structural collapses. Thus, the structural robustness plays a critical role in the TC adsorption.

### 3.1.5. FT-IR Spectroscopy

To confirm the molecular structure and functional groups, FT-IR analysis of the synthesized UiO-66 and UiO-66-NH<sub>2</sub> was performed. As shown in Figure 4, for UiO-66, the band observed at around 1350–1650 cm<sup>−1</sup> corresponds to the asymmetric and symmetric stretching of the C=C and C–O bonds, and the bands at around 860–1170 cm<sup>−1</sup> and 650–800 cm<sup>−1</sup> represent the Zr–O bond. The peaks observed at 816, 742, and 665 cm<sup>−1</sup> correspond to the OH and C–H vibrations in the BDC [23,42]. For UiO-66-NH<sub>2</sub>, the

two peaks at 3370 and 3470  $\text{cm}^{-1}$  reflect symmetric and asymmetric stretching of the primary amines. Moreover, the peaks at 1450 and 1270  $\text{cm}^{-1}$  correspond to the N–H and C–N bonds of the aromatic amines, respectively. The band at around 1540–1600  $\text{cm}^{-1}$  is from the –COOH in the BDC, indicating the occurrence of a reaction between the –COOH and  $\text{Zr}^{4+}$  [43,44].

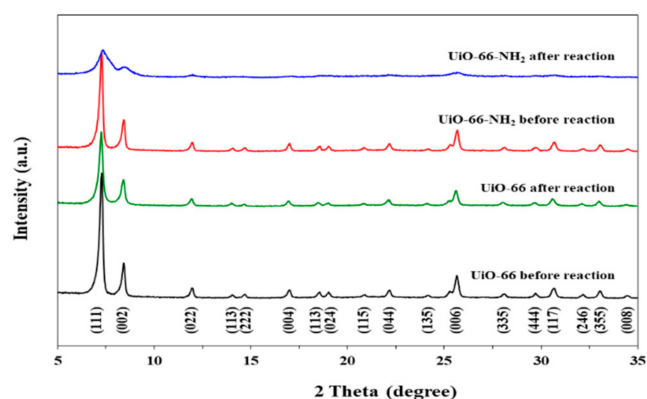


Figure 3. XRD spectra of UiO-66 and UiO-66-NH<sub>2</sub>.

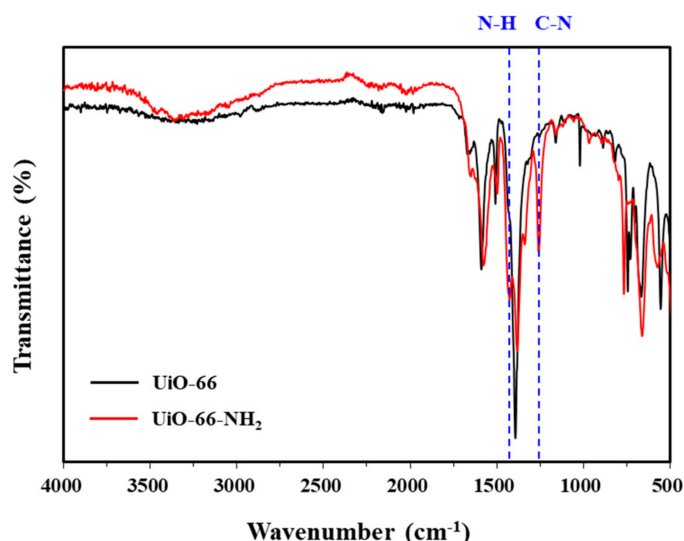


Figure 4. FT-IR spectra of UiO-66 and UiO-66-NH<sub>2</sub> before and after adsorption.

### 3.2. Adsorption Removal of TCs

#### 3.2.1. Batch Adsorption

Before conducting experiments under various conditions, the TC adsorption performance of the synthesized UiO-66 and UiO-66-NH<sub>2</sub> was evaluated. The tests were carried out in 50 mL conical tubes containing 40 mL of 100  $\text{mg L}^{-1}$  TC solution with 20 mg of MOFs for 24 h. The results are presented in Figure S4. The TC adsorption capacities were 65.4  $\text{mg g}^{-1}$  for UiO-66 and 40.2  $\text{mg g}^{-1}$  for UiO-66-NH<sub>2</sub>, indicating that UiO-66 has better adsorption performance than UiO-66-NH<sub>2</sub>.

#### 3.2.2. Effect of Adsorbent Dosage

To optimize the adsorbent dosage, TC adsorption experiments were conducted with different dosages of UiO-66 and UiO-66-NH<sub>2</sub>. The results are shown in Figure 5a,b. An increase in the dosage of UiO-66 and UiO-66-NH<sub>2</sub> increased the removal efficiency of TCs due to the increased number of adsorption sites. However, when the dosage of UiO-66 and UiO-66-NH<sub>2</sub> increased, the maximum adsorption did not increase with the removal efficiency. In fact, the maximum adsorption decreased once a certain threshold was passed.

At dosages of 10, 50, and 100 mg of UiO-66, the maximum TC adsorption was 93.5, 72.5, and 39.3 mg g<sup>-1</sup>, respectively; at 10, 50, and 100 mg of UiO-66-NH<sub>2</sub>, the maximum TC adsorption was 58.2, 52.8, and 41.3 mg g<sup>-1</sup>, respectively. Therefore, the optimum dosage of UiO-66 and UiO-66-NH<sub>2</sub> was determined to be 10 mg.

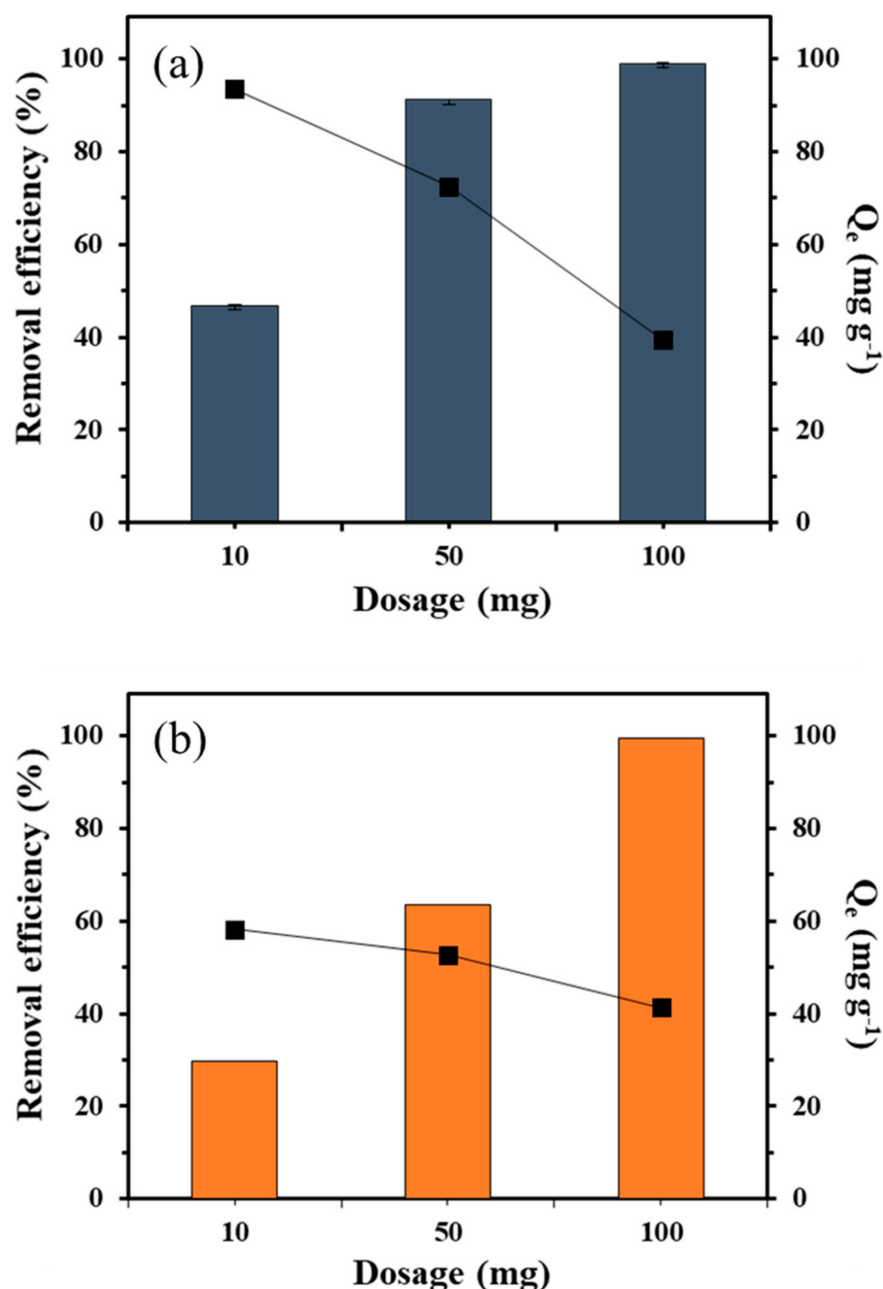


**Figure 5.** Effect of adsorbent dosage on TC adsorption by (a) UiO-66 and (b) UiO-66-NH<sub>2</sub>.

### 3.2.3. Effect of pH and PZC

To understand the adsorption behavior and determine the adsorption mechanism, TC adsorption experiments were conducted under different pH conditions. Figure S5 shows the effect of pH on the adsorption capacity of TCs by UiO-66 and UiO-66-NH<sub>2</sub>. For UiO-66, the adsorption capacity of 90.1 mg g<sup>-1</sup> at pH 3 decreased to 74.9 mg g<sup>-1</sup> as the pH increased. For UiO-66-NH<sub>2</sub>, the adsorption capacity of 52.9 mg g<sup>-1</sup> at pH 3 decreased to 40.4 mg g<sup>-1</sup> with increasing pH. Thus, the maximum adsorption capacity of both UiO-66 and UiO-66-NH<sub>2</sub> was realized at pH 3. The pH affects not only the surface charge of

UiO-66 and UiO-66-NH<sub>2</sub>, but also the degree of TC ionization. Speciation occurs in the TC molecules, which exist as cationic species H<sub>3</sub>TC<sup>+</sup> (pH < 3.3), zwitterionic species H<sub>2</sub>TC<sup>0</sup> (3.3 < pH < 7.7), and anionic species HTC<sup>−</sup> and TC<sup>2−</sup> (pH > 7.7) [45–48]. The pH<sub>pzc</sub> value, representing the electrical balance between the adsorbent surface and the TC solution, was found to be 3 for both UiO-66 and UiO-66-NH<sub>2</sub>; the results are shown in Figure 6. The surfaces of UiO-66 and UiO-66-NH<sub>2</sub> were positively charged at pH < pH<sub>pzc</sub> and negatively charged at pH > pH<sub>pzc</sub>.

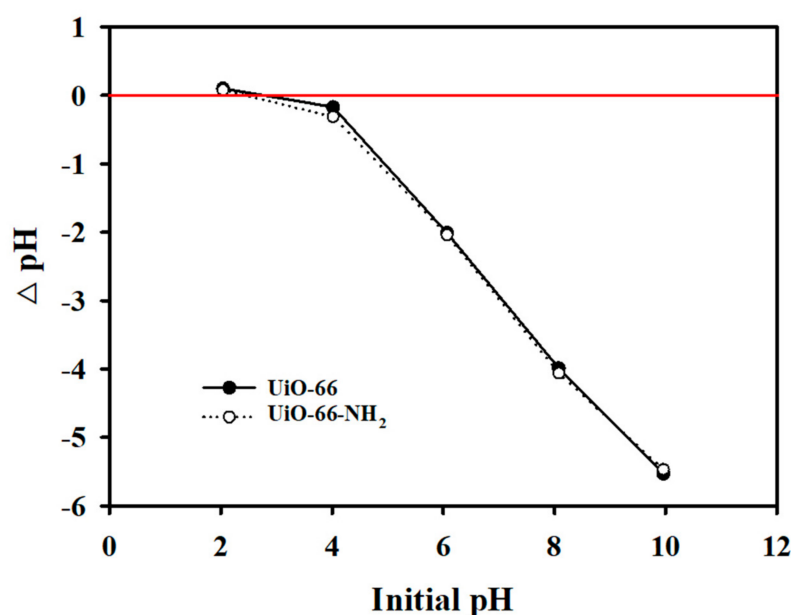


**Figure 6.** Point of zero charge (PZC) for UiO-66 and UiO-66-NH<sub>2</sub>.

### 3.2.4. Effect of Initial TC Concentration and Ionic Strength

Next, experiments were conducted to investigate the effect of the initial TC concentration. The results are presented in Figure S6a,b. The initial TC concentration significantly affected the adsorption. In the case of UiO-66, initial TC concentrations of 10, 25, 50, 75, and 100 mg L<sup>−1</sup> were tested, and the respective removal rates were 92.4%, 76.0%, 42.1%, 31.0%, and 23.1%. In the case of UiO-66-NH<sub>2</sub>, 93.7%, 70.4%, 35.5%, 25.7%, and 18.1% of TCs were removed from the same initial TC concentrations, respectively. For UiO-66, the TC adsorption capacity increased from 38.2 mg g<sup>−1</sup> to 94.3 mg g<sup>−1</sup> as the initial TC concentration increased from 10 mg L<sup>−1</sup> to 100 mg L<sup>−1</sup>. For UiO-66-NH<sub>2</sub>, the TC adsorption capacity increased from 38.7 mg g<sup>−1</sup> to 73.9 mg g<sup>−1</sup> over the same range of initial TC concentrations. As the initial concentration of TCs increased, the concentration gradient driving force increased, which could be the reason for the higher adsorption capacity. We also investigate the effect of coexisting ions, cations and anions, on the TC adsorption efficiency at the low concentration of 0.5 mg L<sup>−1</sup>. Figure S7 shows that TC adsorption efficiency at low concentration is lower than that at high concentration. Furthermore, TC adsorption efficiency decreases in the presence of other ions. Especially, Ca<sup>2+</sup> ions significantly interfered with the TC adsorption for UiO-66-NH<sub>2</sub>.

### 3.2.5. Adsorption Kinetics

Kinetics studies were performed to further explain the effects of UiO-66 and UiO-66-NH<sub>2</sub> on TC adsorption over time. The results are presented in Figure S8a,b. The TCs were rapidly adsorbed in the first 2 h, and the rate then slowed until equilibrium was reached. At pH 3, the TC adsorption capacities were 80.92 mg g<sup>−1</sup> for UiO-66 and 63.7 mg g<sup>−1</sup> for UiO-66-NH<sub>2</sub> at equilibrium. At pH 6, the TC adsorption capacities were 80.47 mg g<sup>−1</sup> for UiO-66 and 42.59 mg g<sup>−1</sup> for UiO-66-NH<sub>2</sub> at equilibrium. Thus, UiO-66 has a higher equilibrium adsorption of TCs than UiO-66-NH<sub>2</sub>. At the beginning of the adsorption tests,



rapid adsorption occurred with all the adsorbents due to the large number of vacant surface sites. As the adsorption time increased, the available sites became saturated and, ultimately, equilibrium was achieved. To understand the adsorption kinetics characteristics of TC onto UiO-66 and UiO-66-NH<sub>2</sub>, pseudo-first- and pseudo-second-order models were applied, as shown in Figure S8a,b. Table 2 presents the related parameters and correlation coefficients for the two models. The pseudo-first-order model can be expressed as:

$$q_t = q_e \left(1 - e^{-k_1 t}\right) \quad (1)$$

where  $q_t$  (mg g<sup>-1</sup>) is the adsorbed amount of the adsorbate at time  $t$ ,  $q_e$  (mg g<sup>-1</sup>) is the uptake of the MOF at equilibrium,  $k_1$  is the pseudo-first-order rate constant (h<sup>-1</sup>), and  $t$  (h) is the adsorption time. The pseudo-second-order model can be expressed as:

$$q_t = \frac{k_2 q_e^2 t}{1 + k_2 q_e t} \quad (2)$$

where  $k_2$  is the pseudo-second-order rate constant (g mg<sup>-1</sup> h<sup>-1</sup>). The adsorption of the TCs onto UiO-66 and UiO-66-NH<sub>2</sub> was adequately described by both the pseudo-first- and pseudo-second-order models, although in general, the pseudo-second-order model produced higher  $R^2$  values. This indicates that chemisorption could be a rate-limiting step in the TC adsorption process.

**Table 2.** Adsorption kinetics parameters of pseudo-first- and pseudo-second-order kinetic equations for TCs on UiO-66 and UiO-66-NH<sub>2</sub>.

Adsorption Kinetic Equations	pH	Constants	UiO-66	UiO-66-NH <sub>2</sub>
Pseudo-first-order rate equation	3	$Q_e$ (mg g <sup>-1</sup> )	$7.48 \times 10^1$	$6.55 \times 10^1$
		$K_1$ (min <sup>-1</sup> )	$2.60 \times 10^{-2}$	$1.04 \times 10^{-2}$
		$R^2$	0.88	0.86
	6	$Q_e$ (mg g <sup>-1</sup> )	$6.24 \times 10^1$	$3.47 \times 10^1$
		$K_1$ (min <sup>-1</sup> )	$3.25 \times 10^{-2}$	$1.57 \times 10^{-2}$
		$R^2$	0.72	0.77
Pseudo-second-order rate equation	3	$Q_e$ (mg g <sup>-1</sup> )	$7.91 \times 10^1$	$6.24 \times 10^1$
		$K_2$ (q mg <sup>-1</sup> min <sup>-1</sup> )	$5.09 \times 10^{-4}$	$3.87 \times 10^{-4}$
		$R^2$	0.95	0.92
	6	$Q_e$ (mg g <sup>-1</sup> )	$6.73 \times 10^1$	$3.63 \times 10^1$
		$K_2$ (q mg <sup>-1</sup> min <sup>-1</sup> )	$6.80 \times 10^{-4}$	$7.45 \times 10^{-4}$
		$R^2$	0.84	0.83

### 3.2.6. Adsorption Isotherms

Adsorption isotherms are useful tools for explaining the distribution of the adsorbates between the liquid and solid when the system has reached equilibrium, and isotherm models show how the interaction between the adsorbent and adsorbate occurs. To understand the adsorption process and compare the TC adsorption abilities of UiO-66 and UiO-66-NH<sub>2</sub>, the Langmuir and Freundlich isotherm model equations were applied. The plots of their nonlinear adjustments are illustrated in Figure S9a,b. The parameter values are listed in Table 3. The Langmuir isotherm model can be expressed as:

$$Q_e = \frac{Q_m K_L C_e}{1 + K_L C_e} \quad (3)$$

**Table 3.** Adsorption kinetics parameters of Langmuir and Freundlich isotherm models for TCs on UiO-66 and UiO-66-NH<sub>2</sub>.

Adsorption Isotherm Model	Constants	UiO-66	UiO-66-NH <sub>2</sub>
Langmuir	$Q_m$ (mg g <sup>−1</sup> )	$9.36 \times 10^1$	$7.65 \times 10^1$
	$K_L$ (L mg <sup>−1</sup> )	3.84	1.57
	$R^2$	0.98	0.97
Freundlich	$K_F$ (mg g <sup>−1</sup> )	$4.92 \times 10^1$	$4.78 \times 10^1$
	$1/n$	$1.61 \times 10^{-1}$	$1.17 \times 10^{-1}$
	$R^2$	0.89	0.81

This equation assumes that the adsorption process occurs on a homogeneous surface where the adsorbate is distributed in monolayers. In this equation,  $Q_e$  is the equilibrium adsorption capacity (mg g<sup>−1</sup>),  $Q_m$  is the maximum adsorption capacity of the adsorbate (mg g<sup>−1</sup>),  $K_L$  is the Langmuir constant (L mg<sup>−1</sup>) indicating the strength of the adsorption capacity, and  $C_e$  is the equilibrium concentration of the adsorbate (mg L<sup>−1</sup>). The Freundlich isotherm model can be expressed as:

$$Q_e = K_F C_e^{\frac{1}{n}} \quad (4)$$

This equation assumes that the adsorption process occurs on a heterogeneous surface through a multilayer adsorption mechanism, and the adsorption capacity correlates with the concentration of TCs at equilibrium. In this equation,  $K_F$  (mg g<sup>−1</sup>) and  $n$  are the adsorption constants that reflect the adsorption capacity. Good adsorption conditions are indicated by  $0 \leq 1/n \leq 1.0$  [49,50]. As shown in Figure S9a,b, the adsorption capacities of UiO-66 and UiO-66-NH<sub>2</sub> increase with increasing TC concentration until the maximum adsorption capacities are achieved. The adsorption of TCs onto UiO-66 and UiO-66-NH<sub>2</sub> are in good agreement with the Langmuir isotherm model:  $R^2$  0.98 for UiO-66 and 0.97 for UiO-66-NH<sub>2</sub>, which are higher than for the Freundlich isotherm model. This suggests that the adsorption behavior was better described by the Langmuir isotherm model. The Langmuir isotherm model is based on monolayer adsorption on the adsorbent surface containing a limited number of adsorptive sites of uniform energy. Thereby, the adsorption of TCs on UiO-66 and UiO-66-NH<sub>2</sub> is considered to be monolayer molecular adsorption.

### 3.3. DFT Calculations

Figure 7 shows the optimized pore structures of UiO-66 and UiO-66-NH<sub>2</sub>, where the pore sizes are too small for TC to penetrate. As the edges of the nanoparticles become smoother after TC adsorption, the TCs would mainly be adsorbed on the surface of the MOF. In contrast to the adsorption trends of adsorbates such as Cr(VI), CO<sub>2</sub>, and CH<sub>4</sub> with UiO-66 and UiO-66-NH<sub>2</sub>, the TC adsorption capacity of UiO-66-NH<sub>2</sub> is lower than that of UiO-66 [51,52]. Even though the −NH<sub>2</sub> functional group has been widely used to improve the adsorption capacity, the introduction of this group onto UiO-66 inhibited TC adsorption capacity. Furthermore, the UiO-66-NH<sub>2</sub> framework severely collapses after the TC adsorption. This could be caused by the weak binding between the organic linker and the metal part. Previous studies examined the structural stability of UiO-66 and UiO-66-NH<sub>2</sub> through temperature gradient analysis (TGA) and found that UiO-66-NH<sub>2</sub> is less stable than UiO-66 [11,34]. Hence, the collapse of the framework would cause a decrease in adsorption capacity by passivating the adsorption sites in the metal clusters [23].

To understand the structural stability of UiO-66 and UiO-66-NH<sub>2</sub>, we conducted DFT calculations using VASP. Figure 8 shows the optimized structures of UiO-66 and UiO-66-NH<sub>2</sub>, indicating the presence of one metal cluster with twelve linkers. In Figure 8b, one of the H atoms in the −NH<sub>2</sub> group and an O atom in the metal cluster (O<sub>H</sub>) form a hydrogen

bond in UiO-66-NH<sub>2</sub>. This causes discrepancies in the charge distributions between O atoms in the metal cluster, and the hydrogen-bonded O atom possesses more electrons than O atoms without hydrogen bonding by 0.2e. Hence, the two Zr-O bonds connecting the organic linker and the metal cluster are not equivalent in UiO-66-NH<sub>2</sub>, which weakens the structural robustness of UiO-66-NH<sub>2</sub> compared to that of UiO-66.

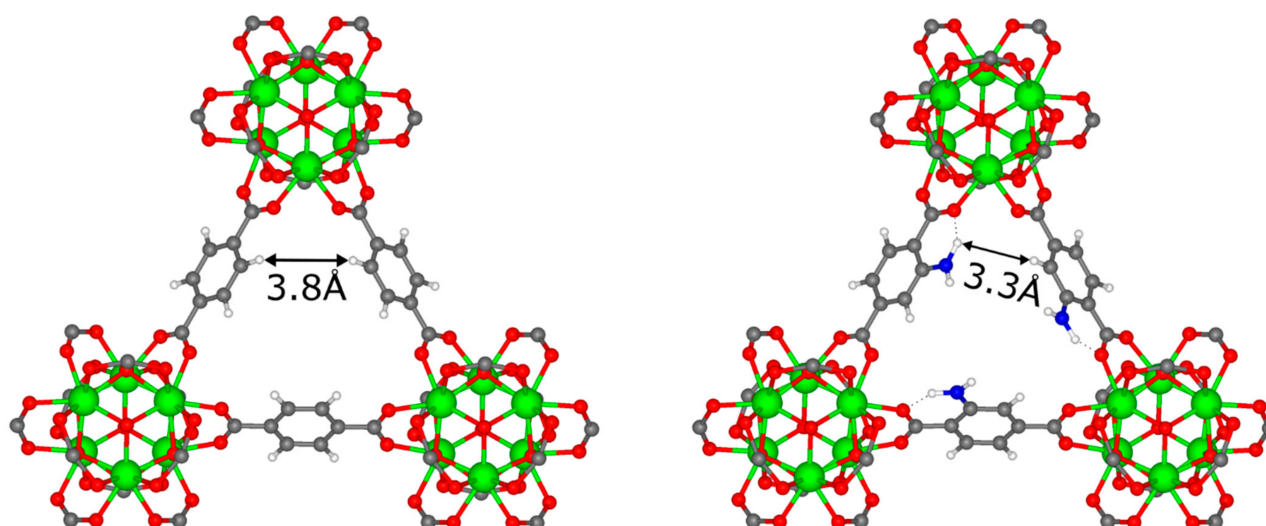


Figure 7. Pore structures of UiO-66 and UiO-66-NH<sub>2</sub>.

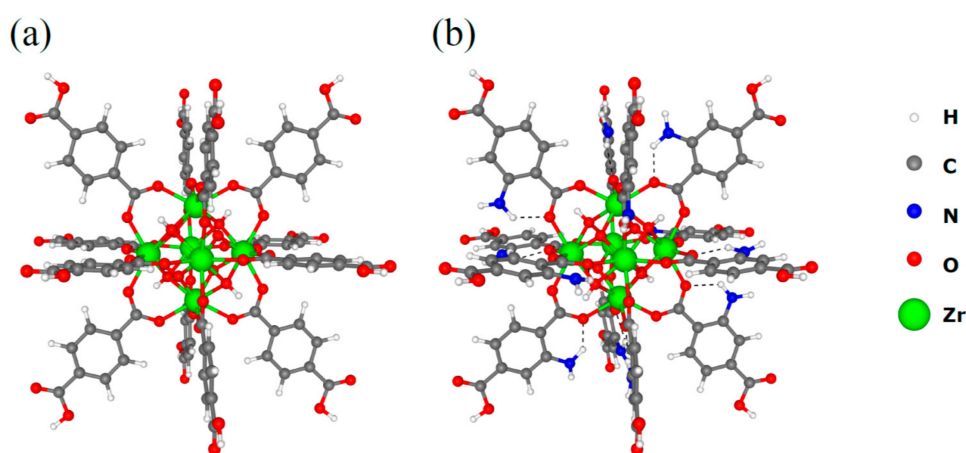


Figure 8. Optimized structures of (a) UiO-66 and (b) UiO-66-NH<sub>2</sub>. Dashed lines indicate hydrogen bonding between O and H atoms. O atoms with and without hydrogen bonding in the metal cluster possess 6.90e and 6.71e, respectively.

#### 4. Conclusions

In this work, the metal organic structures UiO-66 and UiO-66-NH<sub>2</sub> were synthesized to evaluate their performance as adsorbents for the removal of antibiotic TCs in water. The successful synthesis of UiO-66 and UiO-66-NH<sub>2</sub> was confirmed by comparing their BET, XPS, FE-SEM, XRD, and FT-IR characteristic analyses with those in the literature. A kinetics study confirmed that TC was rapidly adsorbed at the beginning of the reaction, and a pseudo-first-order model and Langmuir isotherm model were confirmed to be the most suitable. UiO-66-NH<sub>2</sub> showed lower TC adsorption capacity than UiO-66. DFT calculations showed that the hydrogen bonding between the -NH<sub>2</sub> functional group in the organic linker and the O atoms in the metal cluster weakens the robustness of the framework, and hence the TC adsorption capacity in UiO-66-NH<sub>2</sub> decreases due to the passivation of the adsorption sites in the metal cluster, which is consistent with the experimental analyses.

This study suggests that the robustness of MOFs for preserving adsorption sites during TC adsorption plays a crucial role in their high TC adsorption capacity.

**Supplementary Materials:** The following are available online at <https://www.mdpi.com/article/10.3390/w13131869/s1>. Table S1: Studies for the removal of TCs by adsorption, Table S2: Profiles of MOFs for experimental synthesis, Figure S1: Chemical structures of UiO-66 and UiO-66-NH<sub>2</sub>, Figure S2: Photographs of (a) UiO-66 and (b) UiO-66-NH<sub>2</sub> powders, Figure S3: FE-SEM images of UiO-66 (a) before and (b) after adsorption, and UiO-66-NH<sub>2</sub> (c) before and (d) after adsorption, Figure S4: Adsorption capacity of TCs by UiO-66 and UiO-66-NH<sub>2</sub>, Figure S5: Effect of pH on the adsorption capacity of TCs, Figure S6: Effect of different initial TC concentrations on (a) UiO-66 and (b) UiO-66-NH<sub>2</sub>, Figure S7: Comparison of the effect of ionic strength on TC adsorption at low initial concentration condition, Figure S8: Adsorption kinetics corresponding to the pseudo-first- and pseudo-second-order models of TCs on (a) UiO-66 and (b) UiO-66-NH<sub>2</sub> at different pH values, Figure S9: Adsorption isotherms corresponding to the Langmuir and Freundlich models of TCs on (a) UiO-66 and (b) UiO-66-NH<sub>2</sub>, Figure S10: Particle size distribution of TC.

**Author Contributions:** J.-W.C.: conceptualization, formal analysis, validation, review, editing, supervision, funding acquisition. K.-W.J.: formal analysis, review. H.-G.K.: experiment, writing—original draft. K.C.: density functional theory calculations, review. S.L.: formal analysis. K.L.: review. All authors have read and agreed to the published version of the manuscript.

**Funding:** This research received no external funding.

**Institutional Review Board Statement:** Not applicable.

**Informed Consent Statement:** Not applicable.

**Data Availability Statement:** Data is contained within the article and supplementary material.

**Acknowledgments:** This research was supported by National R&D Program through the National Research Foundation of Korea (NRF) funded by Ministry of Science and ICT (NRF-2020M3H4A3106366) and Ministry of Education (NRF-2020R1I1A1A01073779).

**Conflicts of Interest:** The authors declare that they have no known competing financial interests or personal relationships that could have appeared to influence the work reported in this paper.

## Abbreviations

BET	Brunauer-Emmett-Teller
DFT	Density functional theory
HPLC	High-performance liquid chromatography
MOF	Metal organic framework
OA	Oxalic acid
PAW	Projector-augmented wave
PZC	Point of zero charge
TGA	Temperature Gradient Analysis
VASP	Vienna ab initio Simulation Package
XPS	X-ray photoelectron spectroscopy
XRD	X-ray diffraction
BDC	Terephthalic acid (Benzene-1, 4-dicarboxylic acid, H <sub>2</sub> BDC)
DI	Deionized water
GGA	Generalized gradient approximation
TC	Tetracycline
PTFE	Polytetrafluoroethylene
UV	Ultraviolet

## References

1. Daghrir, R.; Drogui, P. Tetracycline antibiotics in the environment: A review. *Environ. Chem. Lett.* **2013**, *11*, 209–227. [[CrossRef](#)]
2. Li, N.; Zhou, L.; Jin, X.; Owens, G.; Chen, Z. Simultaneous removal of tetracycline and oxytetracycline antibiotics from wastewater using a ZIF-8 metal organic-framework. *J. Hazard. Mater.* **2019**, *366*, 563–572. [[CrossRef](#)]

3. Christian, T.; Schneider, R.J.; Färber, H.A.; Skutlarek, D.; Meyer, M.T.; Goldbach, H.E. Determination of Antibiotic Residues in Manure, Soil, and Surface Waters. *Acta Hydrochim. Hydrobiol.* **2003**, *31*, 36–44. [\[CrossRef\]](#)
4. Göbel, A.; Thomsen, A.; McArdell, C.S.; Joss, A.; Giger, W. Occurrence and Sorption Behavior of Sulfonamides, Macrolides, and Trimethoprim in Activated Sludge Treatment. *Environ. Sci. Technol.* **2005**, *39*, 3981–3989. [\[CrossRef\]](#)
5. Kim, S.-C.; Carlson, K. Temporal and Spatial Trends in the Occurrence of Human and Veterinary Antibiotics in Aqueous and River Sediment Matrices. *Environ. Sci. Technol.* **2007**, *41*, 50–57. [\[CrossRef\]](#)
6. Kummerer, K. Antibiotics in the aquatic environment—A review—Part I. *Chemosphere* **2009**, *75*, 417–434. [\[CrossRef\]](#)
7. Yu, L.-L.; Cao, W.; Wu, S.-C.; Yang, C.; Cheng, J.-H. Removal of tetracycline from aqueous solution by MOF/graphite oxide pellets: Preparation, characteristic, adsorption performance and mechanism. *Ecotoxicol. Environ. Saf.* **2018**, *164*, 289–296. [\[CrossRef\]](#)
8. Hu, T.; Jia, Q.; He, S.; Shan, S.; Su, H.; Zhi, Y.; He, L. Novel functionalized metal-organic framework MIL-101 adsorbent for capturing oxytetracycline. *J. Alloy. Compd.* **2017**, *727*, 114–122. [\[CrossRef\]](#)
9. Miège, C.; Choubert, J.-M.; Ribeiro, L.; Eusèbe, M.; Coquery, M. Fate of pharmaceuticals and personal care products in wastewater treatment plants—Conception of a database and first results. *Environ. Pollut.* **2009**, *157*, 1721–1726. [\[CrossRef\]](#)
10. González-Ortiz, A.; Ramírez-García, J.J.; Solache-Ríos, M.J. Kinetic and Thermodynamic Behavior on the Sorption of Clindamycin from an Aqueous Medium by Modified Surface Zeolitic Tuffs. *Water Air Soil Pollut.* **2018**, *229*. [\[CrossRef\]](#)
11. Cao, Y.; Zhang, H.; Song, F.; Huang, T.; Ji, J.; Zhong, Q.; Chu, W.; Xu, Q. UiO-66-NH<sub>2</sub>/GO Composite: Synthesis, Characterization and CO<sub>2</sub> Adsorption Performance. *Materials* **2018**, *11*, 589. [\[CrossRef\]](#)
12. Bautitz, I.R.; Nogueira, R.F.P. Degradation of tetracycline by photo-Fenton process—Solar irradiation and matrix effects. *J. Photochem. Photobiol. A: Chem.* **2007**, *187*, 33–39. [\[CrossRef\]](#)
13. Kim, I.; Tanaka, H. Photodegradation characteristics of PPCPs in water with UV treatment. *Environ. Int.* **2009**, *35*, 793–802. [\[CrossRef\]](#)
14. Peñalver, J.J.L.; Sanchez-Polo, M.; Gómez-Pacheco, C.V.; Rivera-Utrilla, J. Photodegradation of tetracyclines in aqueous solution by using UV and UV/H<sub>2</sub>O<sub>2</sub> oxidation processes. *J. Chem. Technol. Biotechnol.* **2010**, *85*, 1325–1333. [\[CrossRef\]](#)
15. Wang, P.; He, Y.-L.; Huang, C.-H. Reactions of tetracycline antibiotics with chlorine dioxide and free chlorine. *Water Res.* **2011**, *45*, 1838–1846. [\[CrossRef\]](#)
16. Batt, A.L.; Kim, S.; Aga, D.S. Comparison of the occurrence of antibiotics in four full-scale wastewater treatment plants with varying designs and operations. *Chemosphere* **2007**, *68*, 428–435. [\[CrossRef\]](#) [\[PubMed\]](#)
17. Watkinson, A.; Murby, E.; Costanzo, S. Removal of antibiotics in conventional and advanced wastewater treatment: Implications for environmental discharge and wastewater recycling. *Water Res.* **2007**, *41*, 4164–4176. [\[CrossRef\]](#) [\[PubMed\]](#)
18. Chao, Y.; Zhu, W.; Chen, F.; Wang, P.; Da, Z.; Wu, X.; Ji, H.; Yan, S.; Li, H. Commercial Diatomite for Adsorption of Tetracycline Antibiotic from Aqueous Solution. *Sep. Sci. Technol.* **2014**, *49*, 2221–2227. [\[CrossRef\]](#)
19. Kang, J.; Liu, H.; Zheng, Y.-M.; Qu, J.; Chen, J.P. Application of nuclear magnetic resonance spectroscopy, Fourier transform infrared spectroscopy, UV-Visible spectroscopy and kinetic modeling for elucidation of adsorption chemistry in uptake of tetracycline by zeolite beta. *J. Colloid Interface Sci.* **2011**, *354*, 261–267. [\[CrossRef\]](#)
20. Yaghi, O.; Li, G.; Li, H. Selective binding and removal of guests in a microporous metal-organic framework. *Nat. Cell Biol.* **1995**, *378*, 703–706. [\[CrossRef\]](#)
21. Bai, Y.; Dou, Y.; Xie, L.-H.; Rutledge, W.; Li, J.-R.; Zhou, H.-C. Zr-based metal-organic frameworks: Design, synthesis, structure, and applications. *Chem. Soc. Rev.* **2016**, *45*, 2327–2367. [\[CrossRef\]](#) [\[PubMed\]](#)
22. Carboni, M.; Abney, C.; Liu, S.; Lin, W. Highly porous and stable metal-organic frameworks for uranium extraction. *Chem. Sci.* **2013**, *4*, 2396–2402. [\[CrossRef\]](#)
23. Chen, C.; Chen, D.; Xie, S.; Quan, H.; Luo, X.; Guo, L. Adsorption behaviors of organic micropollutants on zirconium metal-organic framework UiO-66: Analysis of surface interactions. *ACS Appl. Mater. Interfaces* **2017**, *9*, 41043–41054. [\[CrossRef\]](#) [\[PubMed\]](#)
24. Feng, D.; Chung, W.-C.; Wei, Z.; Gu, Z.-Y.; Jiang, H.-L.; Chen, Y.-P.; Darenbourg, D.J.; Zhou, H.-C. Construction of Ultrastable Porphyrin Zr Metal-Organic Frameworks through Linker Elimination. *J. Am. Chem. Soc.* **2013**, *135*, 17105–17110. [\[CrossRef\]](#)
25. Gutov, O.V.; Bury, W.; Gomez-Gualdron, D.A.; Krungleviciute, V.; Fairen-Jimenez, D.; Mondloch, J.E.; Sarjeant, A.A.; Al-Juaid, S.S.; Snurr, R.Q.; Hupp, J.T.; et al. Water-stable zirconium-based metal-organic framework material with high-surface area and gas-storage capacities. *Chem. Eur. J.* **2014**, *20*, 12389–12393. [\[CrossRef\]](#) [\[PubMed\]](#)
26. Mondloch, J.E.; Bury, W.; Fairen-Jimenez, D.; Kwon, S.; DeMarco, E.J.; Weston, M.H.; Sarjeant, A.A.; Nguyen, S.; Stair, P.C.; Snurr, R.; et al. Vapor-Phase Metalation by Atomic Layer Deposition in a Metal-Organic Framework. *J. Am. Chem. Soc.* **2013**, *135*, 10294–10297. [\[CrossRef\]](#)
27. Taddei, M. When defects turn into virtues: The curious case of zirconium-based metal-organic frameworks. *Coord. Chem. Rev.* **2017**, *343*. [\[CrossRef\]](#)
28. Wu, H.; Yildirim, T.; Zhou, W. Exceptional Mechanical Stability of Highly Porous Zirconium Metal-Organic Framework UiO-66 and Its Important Implications. *J. Phys. Chem. Lett.* **2013**, *4*, 925–930. [\[CrossRef\]](#)
29. Yang, Z.-H.; Cao, J.; Chen, Y.-P.; Li, X.; Xiong, W.-P.; Zhou, Y.-Y.; Zhou, C.-Y.; Xu, R.; Zhang, Y.-R. Mn-doped zirconium metal-organic framework as an effective adsorbent for removal of tetracycline and Cr(VI) from aqueous solution. *Microporous Mesoporous Mater.* **2019**, *277*, 277–285. [\[CrossRef\]](#)



30. Cavka, J.H.; Jakobsen, S.; Olsbye, U.; Guillou, N.; Lamberti, C.; Bordiga, S.; Lillerud, K.P. A New Zirconium Inorganic Building Brick Forming Metal Organic Frameworks with Exceptional Stability. *J. Am. Chem. Soc.* **2008**, *130*, 13850–13851. [\[CrossRef\]](#)
31. Huang, A.; Wan, L.; Caro, J. Microwave-assisted synthesis of well-shaped UiO-66-NH<sub>2</sub> with high CO<sub>2</sub> adsorption capacity. *Mater. Res. Bull.* **2018**, *98*, 308–313. [\[CrossRef\]](#)
32. Feng, Y.; Chen, Q.; Jiang, M.; Yao, J. Tailoring the Properties of UiO-66 through Defect Engineering: A Review. *Ind. Eng. Chem. Res.* **2019**, *58*, 17646–17659. [\[CrossRef\]](#)
33. Cao, J.; Yang, Z.-H.; Xiong, W.-P.; Zhou, Y.-Y.; Peng, Y.-R.; Li, X.; Zhou, C.-Y.; Xu, R.; Zhang, Y.-R. One-step synthesis of Co-doped UiO-66 nanoparticle with enhanced removal efficiency of tetracycline: Simultaneous adsorption and photocatalysis. *Chem. Eng. J.* **2018**, *353*, 126–137. [\[CrossRef\]](#)
34. Katz, M.J.; Brown, Z.J.; Colón, Y.J.; Siu, P.W.; Scheidt, K.; Snurr, R.; Hupp, J.T.; Farha, O.K. A facile synthesis of UiO-66, UiO-67 and their derivatives. *Chem. Commun.* **2013**, *49*, 9449–9451. [\[CrossRef\]](#)
35. Kresse, G.; Furthmüller, J. Efficiency of ab-initio total energy calculations for metals and semiconductors using a plane-wave basis set. *Comput. Mater. Sci.* **1996**, *6*, 15–50. [\[CrossRef\]](#)
36. Kresse, G.; Furthmüller, J. Efficient iterative schemes for ab initio total-energy calculations using a plane-wave basis set. *Phys. Rev. B Condens. Matter* **1996**, *54*. [\[CrossRef\]](#)
37. Perdew, J.P.; Burke, K.; Ernzerhof, M. Generalized gradient approximation made simple. *Phys. Rev. Lett.* **1996**, *77*, 3865–3868. [\[CrossRef\]](#)
38. Blöchl, P.E. Projector augmented-wave method. *Phys. Rev. B Condens. Matter* **1994**, *50*. [\[CrossRef\]](#)
39. Henkelman, G.; Arnaldsson, A.; Jónsson, H. A fast and robust algorithm for Bader decomposition of charge density. *Comput. Mater. Sci.* **2006**, *36*, 354–360. [\[CrossRef\]](#)
40. Momma, K.; Izumi, F. VESTA: A three-dimensional visualization system for electronic and structural analysis. *J. Appl. Crystallogr.* **2008**, *41*, 653–658. [\[CrossRef\]](#)
41. Zhang, Y.; Ruan, Q.; Peng, Y.; Han, G.; Huang, H.; Zhong, C. Synthesis of hierarchical-pore metal-organic framework on liter scale for large organic pollutants capture in wastewater. *J. Colloid Interface Sci.* **2018**, *525*, 39–47. [\[CrossRef\]](#)
42. Tong, X.; Yang, Z.; Feng, J.; Li, Y.; Zhang, H. BiOCl/UiO-66 composite with enhanced performance for photo-assisted degradation of dye from water. *Appl. Organomet. Chem.* **2018**, *32*. [\[CrossRef\]](#)
43. Wang, Y.; Chen, H.; Hu, X.; Yu, H. Highly stable and ultrasensitive chlorogenic acid sensor based on metal–organic frameworks/titanium dioxide nanocomposites. *Analyst* **2016**, *141*, 4647–4653. [\[CrossRef\]](#) [\[PubMed\]](#)
44. Cho, K.Y.; Seo, J.Y.; Kim, H.-J.; Pai, S.J.; Do, X.H.; Yoon, H.G.; Hwang, S.S.; Han, S.S.; Baek, K.-Y. Facile control of defect site density and particle size of UiO-66 for enhanced hydrolysis rates: Insights into feasibility of Zr(IV)-based metal-organic framework (MOF) catalysts. *Appl. Catal. B Environ.* **2019**, *245*, 635–647. [\[CrossRef\]](#)
45. Duan, L.; Li, L.; Xu, Z.; Chen, W. Adsorption of tetracycline to nano-NiO: The effect of coexisting Cu(II) ions and environmental implications. *Environ. Sci. Process Impacts* **2014**, *16*, 1462–1468. [\[CrossRef\]](#)
46. Qin, Q.; Wu, X.; Chen, L.; Jiang, Z.; Xu, Y. Simultaneous removal of tetracycline and Cu(II) by adsorption and coadsorption using oxidized activated carbon. *RSC Adv.* **2018**, *8*, 1744–1752. [\[CrossRef\]](#)
47. Zhao, Y.; Geng, J.; Wang, X.; Gu, X.; Gao, S. Adsorption of tetracycline onto goethite in the presence of metal cations and humic substances. *J. Colloid Interface Sci.* **2011**, *361*, 247–251. [\[CrossRef\]](#) [\[PubMed\]](#)
48. Ma, X.; Xin, Y.; Yan, Q.; Pan, X.; Xin, S.; Huang, X.; Chen, Q.; Liu, G. Adsorption Characteristics of Tetracycline onto Biochars as Affected by Solution Chemistry Conditions and Ball Milling Treatment. *Water Air Soil Pollut.* **2020**, *231*. [\[CrossRef\]](#)
49. Fang, Y.; Wen, J.; Zeng, G.; Jia, F.; Zhang, S.; Peng, Z.; Zhang, H. Effect of mineralizing agents on the adsorption performance of metal–organic framework MIL-100(Fe) towards chromium(VI). *Chem. Eng. J.* **2018**, *337*, 532–540. [\[CrossRef\]](#)
50. Wang, D.; Jia, F.; Wang, H.; Chen, F.; Fang, Y.; Dong, W.; Zeng, G.; Li, X.; Yang, Q.; Yuan, X. Simultaneously efficient adsorption and photocatalytic degradation of tetracycline by Fe-based MOFs. *J. Colloid Interface Sci.* **2018**, *519*, 273–284. [\[CrossRef\]](#)
51. Luu, C.L.; Van Nguyen, T.T.; Nguyen, T.; Hoang, T.C. Synthesis, characterization and adsorption ability of UiO-66-NH<sub>2</sub>. *Adv. Nat. Sci. Nanosci. Nanotechnol.* **2015**, *6*. [\[CrossRef\]](#)
52. Wu, S.; Ge, Y.; Wang, Y.; Chen, X.; Li, F.; Xuan, H.; Li, X. Adsorption of Cr(VI) on nano UiO-66-NH<sub>2</sub> MOFs in water. *Environ. Technol.* **2018**, *39*, 1937–1948. [\[CrossRef\]](#) [\[PubMed\]](#)